Title

Optical imaging of the chorioretinal vasculature in the living human eye.

Journal

Proceedings of the National Academy of Sciences of the United States of America, 110(35)

ISSN

0027-8424

Authors

Kim, Dae Yu
Fingler, Jeff
Zawadzki, Robert J
et al.

Publication Date

2013-08-01

DOI

10.1073/pnas.1307315110

Peer reviewed

Optical imaging of the chorioretinal vasculature in the living human eye

Dae Yu Kim[a], Jeff Fingler[a], Robert J. Zawadzki[b], Susanna S. Park[b], Lawrence S. Morse[b], Daniel M. Schwartz[c], Scott E. Fraser[a,1], and John S. Werner[b,1]

[a]Biological Imaging Center, California Institute of Technology, Pasadena, CA 91125; [b]Department of Ophthalmology and Vision Science, University of California, Davis, Sacramento, CA 95817; and [c]Department of Ophthalmology, University of California, San Francisco, CA 94143

Edited* by Napoleone Ferrara, University of California, San Diego, La Jolla, CA, and approved July 9, 2013 (received for review April 18, 2013)

Detailed visualization of microvascular changes in the human retina is clinically limited by the capabilities of angiography imaging, a 2D fundus photograph that requires an intravenous injection of fluorescent dye. Whereas current angiography methods enable visualization of some retinal capillary detail, they do not adequately reveal the choriocapillaris or other microvascular features beneath the retina. We have developed a noninvasive microvascular imaging technique called phase-variance optical coherence tomography (pvOCT), which identifies vasculature three dimensionally through analysis of data acquired with OCT systems. The pvOCT imaging method is not only capable of generating capillary perfusion maps for the retina, but it can also use the 3D capabilities to segment the data in depth to isolate vasculature in different layers of the retina and choroid. This paper demonstrates some of the capabilities of pvOCT imaging of the anterior layers of choroidal vasculature of a healthy normal eye as well as of eyes with geographic atrophy (GA) secondary to age-related macular degeneration. The pvOCT data presented permit digital segmentation to produce 2D depth-resolved images of the retinal vasculature, the choriocapillaris, and the vessels in Sattler's and Haller's layers. Comparisons are presented between *en face* projections of pvOCT data within the superficial choroid and clinical angiography images for regions of GA. Abnormalities and vascular dropout observed within the choriocapillaris for pvOCT are compared with regional GA progression. The capability of pvOCT imaging of the microvasculature of the choriocapillaris and the anterior choroidal vasculature has the potential to become a unique tool to evaluate therapies and understand the underlying mechanisms of age-related macular degeneration progression.

ocular circulation | ocular vasculature | optical angiography | ophthalmic imaging | Fourier-domain optical coherence tomography

Current clinical evaluation of outer retinal disease progression is accomplished with multiple imaging modalities including fundus photography, fluorescein angiography (FA), indocyanine green angiography (ICGA), fundus autofluorescence (FAF), and near infrared autofluorescence (1, 2). Whereas angiography techniques are ideal to observe retinal and choroidal circulation, the lack of depth selectivity limits the ability to observe microvasculature in the choriocapillaris (CC) and the anterior choroid. FA is typically limited to retinal vasculature due to light absorption by the retinal pigment epithelial (RPE) cells and leakage of fluorescein from the choriocapillaris, whereas ICGA primarily images only the larger choroidal vessels. The development of a unique noninvasive method for visualizing changes in the RPE layer and CC with high resolution could advance our understanding of disease progression and invites unique opportunities for early diagnosis, timely treatment, and evaluating potential therapeutics.

One of the major applications of noninvasive choroidal imaging is for late stages of age-related macular degeneration (AMD), the leading cause of central visual loss and legal blindness in Americans 65 y of age and older (3). Geographic atrophy (GA), one of the common features of AMD, involves the progressive loss of the retinal photoreceptors and the RPE cells, as well as atrophy of the underlying CC and choroidal vessels (4–6). GA regional identification is typically accomplished using autofluorescence imaging techniques, which depend on lipofuscin accumulation within RPE cells associated with this disease, but the current clinical imaging methods are limited in detecting early morphological changes in the choriocapillaris (7, 8). An improved understanding of the progression of GA and its underlying mechanisms is important to develop potential therapeutic targets for intervention, and diagnostic tools capable of observing the key features of atrophic AMD are critical for fulfilling this goal.

Optical coherence tomography (OCT) is a noninvasive clinical diagnostic tool that performs high-resolution (few micrometers), 3D cross-sectional imaging of the retina (9, 10). Current OCT imaging provides detailed retinal morphology that correlates well with histologic findings. Although high-resolution OCT is capable of depicting structural alterations of the outer retinal layers including the RPE layer in patients with atrophic AMD (11), conventional OCT imaging provides limited visualization of the retinal and choroidal circulation. Recently, the enhanced depth imaging technique demonstrated cross-sectional images of choriocapillaris and larger choroidal vessels with improved OCT sensitivity in the choroid to measure choroidal thickness (12, 13). To image retinal and choroidal vasculature noninvasively, we have developed phase-variance optical coherence tomography (pvOCT), which calculates contrast based on the motion observed over time of the 3D OCT data. This additional contrast method allows for in vivo visualization of volumetric morphology of retinal and choroidal microvasculature with high sensitivity as well as presentation of the vascular data in the form of depth-encoded 2D perfusion maps of the retina. A principal benefit of pvOCT for translational research and further clinical applications is that this is a data analysis technique that can be adapted for use by clinically available OCT systems without requiring any hardware modifications. Composite imaging of conventional OCT intensity images and pvOCT images highlights localization of vascular changes in three dimensions, which may allow for more accurate diagnosis of changes in CC that may lead to GA. In addition, disruptions in the photoreceptors and RPE that may be associated with these vascular changes can also be studied simultaneously.

Results

We acquired OCT volumetric data of the macula (posterior retina) of a normal human subject and one AMD patient with GA. Using a custom-built Fourier-domain OCT (Fd-OCT) system, we

Author contributions: D.Y.K., S.E.F., and J.S.W. designed research; D.Y.K., J.F., and R.J.Z. performed research; D.Y.K., S.S.P., L.S.M., and D.M.S. analyzed data; and D.Y.K., J.F., R.J.Z., S.S.P., L.S.M., D.M.S., S.E.F., and J.S.W. wrote the paper.

The authors declare no conflict of interest.

*This Direct Submission article had a prearranged editor.

Freely available online through the PNAS open access option.

[1]To whom correspondence may be addressed. E-mail: jswerner@ucdavis.edu or sefraser@caltech.edu.

This article contains supporting information online at www.pnas.org/lookup/suppl/doi:10.1073/pnas.1307315110/-/DCSupplemental.

performed pvOCT imaging scans over retinal areas of 1.5×1.5 mm^2 and 3×3 mm^2 with an acquisition time of 3.6 s in addition to scans of 1.5×3 mm^2 and 3×1.5 mm^2 acquired in 6.9 s. Healthy retinal areas at the macula and the peripheral retina were imaged for comparison with atrophic areas in AMD. The pvOCT images were created using postprocessing procedures including phase-variance–based analysis to identify motion contrast as well as segmentation of the 3D data for visualizing vasculature both in the retina and the choroid. Details of the phase-variance processing and visualization for pvOCT are described in Fig. S1.

Microcirculation in the Retina and the Choroid. Fundus FA has served as the gold standard for imaging the retinal vasculature and its abnormalities, including but not limited to microaneurysms, capillary nonperfusion, and neovascularization. In addition, fundus ICGA has been mainly used to identify choroidal vascular abnormalities, although it visualizes both retinal and choroidal circulation. Unlike FA, the absorption (~790–800 nm) and emission (~830–840 nm) wavelengths of ICGA are in the near-infrared range, which enables imaging deep choroidal networks below the RPE. By zooming in on fundus FA and ICGA of a 60-y-old male subject with no previous history of ocular disease, vascular networks in the retina (Fig. 1*A*) as well as in the retina and the choroid (Fig. 1*B*) are observed (viewable full size images in Fig. S2). However, these clinical imaging modalities are limited in their ability to visualize the CC, which provides the blood supply to the photoreceptors and may be damaged as AMD progresses. One major difficulty in studying the changes in CC has been its anatomical location below the photoreceptors and the highly pigmented RPE, where most of the incident light is absorbed or scattered. The CC consists of lobules of fenestrated capillary plexus in the macula. These features make CC difficult to visualize by FA and ICGA.

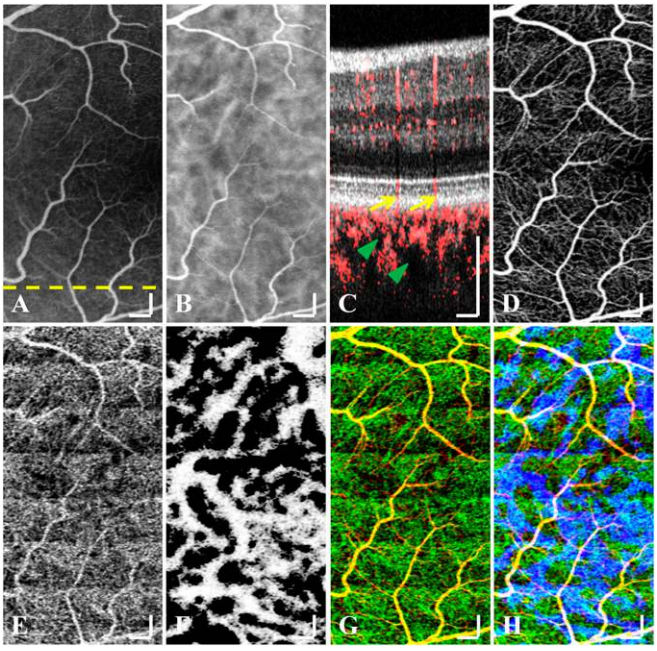

Fig. 1. Comparison of fundus photographs and pvOCT *en face* projection images for a scanning area of 1.5×3 mm^2. Selected regions of FA (*A*) and ICGA (*B*) of a healthy volunteer from large field photographs (Fig. S2). The cross-sectional composite depth image (*C*) of OCT intensity (gray) and pvOCT (red) is presented for the retinal location identified by the yellow dashed line in *A*. *En face* maximum projection of pvOCT data segmented from retinal layers and at a depth of 5.2 μm underneath Bruch's membrane, to present the features of the retinal vessels (*D*) and the choriocapillaris (CC) (*E*), respectively. *En face* projection of pvOCT for retinal vasculature (*D*) demonstrates comparable microvascular visualization to FA (*A*). Inverting intensity of minimum projection (*F*) of the pvOCT data segmented a depth slice of 35 μm thickness, located ~50 μm below the RPE. This inverse image visualizes large feeder vessels in the choroid, where there is usually non–phase-variance signal inside of these vessels shown by green arrowheads in *C*. The color-coded images (*G* and *H*) are combined from retinal vessels (*D*, red), CC (*E*, green), and deep choroidal vessels (*F*, blue). (Scale bars, 200 μm.)

Our OCT angiographic technique, pvOCT, allows in vivo visualization of the retinal and choroidal circulation with depth information. The cross-sectional composite image (Fig. 1*C*) scanned at the retinal location identified by the yellow dashed line in Fig. 1*A* emphasizes vascular depth information (red) available in the retina and the choroid. This cross-sectional (B-scan) image was a combination of the standard Fd-OCT B-scan (Fig. S3*A*) and the phase variance processed contrast for the same location (Fig. S3*B*). An *en face* projection of the pvOCT volumetric data (Movie S1) enables visualization of capillary perfusion maps of different posterior layers. The retinal vasculature (Fig. 1*D*) was segmented from the retinal nerve fiber layer to the outer plexiform layer (yellow dashed rectangle in Fig. S3*C*). The diameter of the smallest retinal capillaries imaged in Fig. 1*D* is ~5–10 μm. In the choroid, there are three layers shown in Fig. S3*A*: the CC underneath Bruch's membrane, Sattler's layer containing medium-sized choroidal vessels, and Haller's layer containing large choroidal vessels and pigmented cells. The CC imaging (Fig. 1*E*) was segmented as a thin depth slice located ~5.2 μm underneath Bruch's membrane (marked by the green dotted rectangle in Fig. S3*C*). The resolved size of CC in Fig. 1*E* is ~20 μm in diameter. Contained within the motion contrast of the lobular capillary plexus are retinal vessel shadow artifacts marked by yellow arrows (Fig. 1*C*), which are caused by imaging below regions of flow with remaining nonzero phase-variance values. As indicated by the green arrowheads (Fig. 1*C*), there is no phase-variance signal inside deep choroidal vessels, whereas the signal is present in surrounding capillary plexuses outside the feeder vessels. To visualize the choroidal vasculature (Fig. 1*F*), an image was created after inversing minimum projection (Fig. S3*D*) of the blue dotted rectangular area (Fig. S3*C*). A composite (Fig. 1*G*) of the retinal vasculature (Fig. 1*D*, red) and the CC (Fig. 1*E*, green) demonstrates distinct features of posterior pole CC. In this superimposed image, some retinal vessels are coded as yellowish instead of red because larger retinal vessels were included in the CC image (Fig. 1*E*) due to the shadow artifacts of the retinal vessels.

An additional scan was performed at the same location (Fig. S4 *A*–*C*) to demonstrate the reproducibility of this imaging method. It should be noted that there appear to be variations in the vascular contrast, particularly in Fig. 1*E*, which present as bright and dim horizontal regions in the image. This banding is present in the horizontal direction in both scans acquired over the same region (Fig. 1 and Fig. S4), where the slow scan direction of the 3D scan is vertical. This variation in the phase-variance signal appears at different positions in the two different scans but with similar spatial frequency, corresponding to this subject's pulse, which caused the nonuniform vascular patterns (Fig. S4*D*). Similarly, the vertical banding of the vascular contrast variations in the pvOCT projection of Fig. 2 occurred because the primary scan direction was oriented 90° relative to the data of Fig. 1.

Choriocapillaris and Vasculature in Sattler's Layer. Anatomical studies of human choroidal circulation have reported that structural patterns and sizes of CC have regional variations over the retina (14, 15). To demonstrate in vivo CC images at different retinal locations, we acquired pvOCT over peripheral retina (6° nasal and 12° inferior retina eccentricities) in the left eye (visual acuity: 20/60) of a 61-y-old female with geographic atrophy in the fovea. The color fundus photograph (Fig. 2*A*) shows no major degeneration in the acquired region denoted by the yellow dotted rectangle in Fig. S5*A*. Highly anastomosed capillary networks (Fig. 2*C*) in CC are included in the fly-

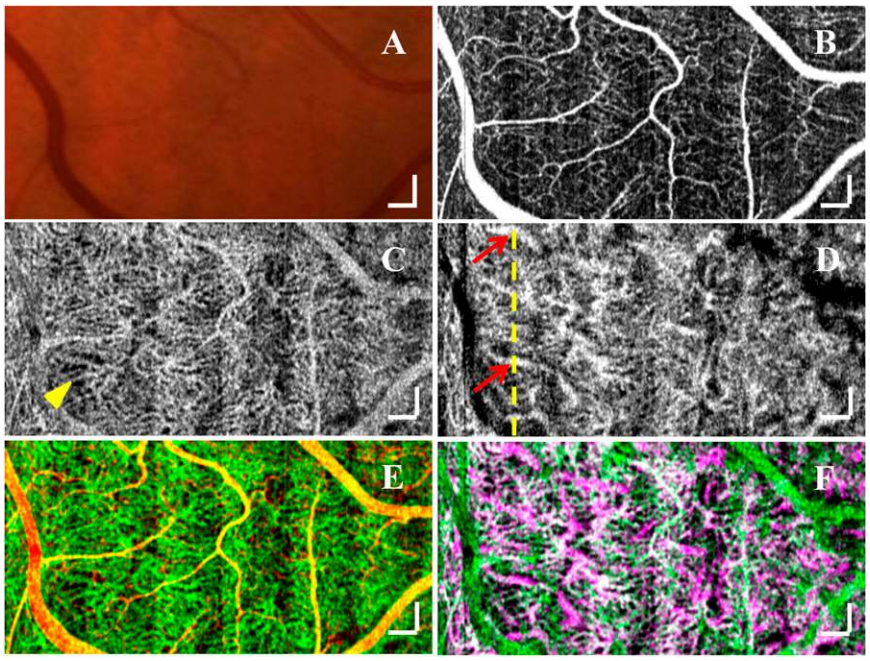

Fig. 2. Imaging of choriocapillaris of the peripheral retina for a scanning area of 3 × 1.5 mm^2 with additional identification of arterioles and venules in the choroid. Color fundus photograph (*A*) zooming in the region of the yellow dotted rectangle in the full-size image (Fig. S5*A*). Maximum projection of pvOCT data from retinal layers (*B*) and CC (*C*) and Sattler's layer (*D*). The yellow dashed line in *D* is shown in cross-sectional views in Fig. 5 *A*–*D*. Segmented depths for these images are positioned 9 μm underneath Bruch's membrane for the CC and 16 μm for Sattler's layer. The color-coded image (*E*) is combined from retinal capillaries (*B*, red) and CC (*C*, green) as well as the image (*F*) consisting of CC (*C*, green) and Sattler's layer (*D*, magenta). (Scale bars, 200 μm.)

through video (Movie S2), ∼230 μm below the anterior surface of the retina. The CC denoted by the yellow arrowhead in Fig. 2*C* is ∼36 μm in diameter. The vessels of Sattler's layer (Fig. 2*D*), located between the CC and Haller's layer (the outermost layer in the choroid), include medium-sized arterioles and venules ∼70–85 μm in diameter at the red arrows. Cross-sectional views (see Fig. 5 *A* and *B*) were acquired at the location identified by the yellow dashed line (Fig. 2*D*), illustrating depth locations of retinal and choroidal circulation. The composite image (Fig. 2*E*) accentuates the highly dense capillary plexus of CC (Fig. 2*C*, green) visualized with the retinal circulation (Fig. 2*B*, red), available to exhibit lobular patterns of CC (Fig. S6 and Movie S7). In addition, the superimposed image (Fig. 2*F*) of the CC (Fig. 2*C*, green) and choroidal vessels of the intermediate layer (Fig. 2*D*, magenta) demonstrates medium-sized vessel networks supplying the CC. Morphological features of these in vivo results are analogous to the histological images by corrosion vascular casts and scanning electron microscopy (14).

Abnormalities in the Choroidal Circulation: GA. Although current clinical imaging modalities can define progression of GA in eyes with AMD for large and well-established lesions, there is little information available regarding changes in the CC in the early stages of the disease (8). One of the reasons has been the limited ability to study in vivo changes in CC in detail thus far. The clinical images (Fig. 3 *A*–*D*) from the GA patient shown in Fig. 2 identify the atrophic regions at the fovea (3° inferior retina eccentricities) by different methods. The color (Fig. 3*A*) and red-

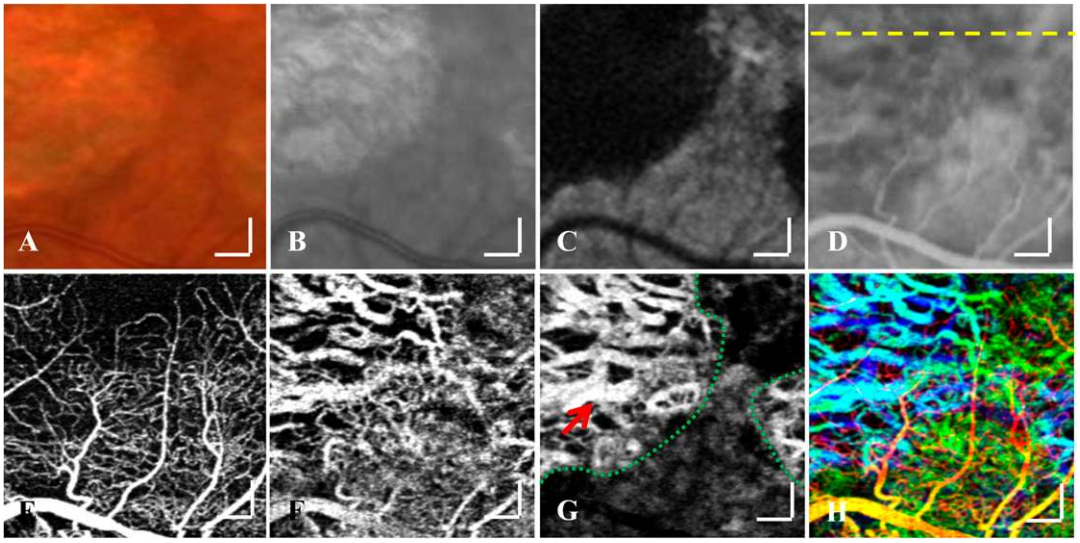

Fig. 3. Small field of view images (1.5 × 1.5 mm^2) at the atrophic region of the patient with GA. Selected regions of color fundus (*A*), red-free (*B*), AF (*C*), and the early venous stage of FA (*D*) images from the location identified in the green square (Fig. S5). The yellow dashed line in *D* is shown in cross-sectional views in Fig. 6 *E*–*H*. *En face* projection images for retinal vasculature (*E*), vessels in the inner choroidal layer (*F*), and large choroidal vessels (*G*) from pvOCT data (Movie S3). A composite image (*H*) of three depth layers (retina, red; inner choroid, green; deep choroid, blue). (Scale bars, 200 μm.)

free (Fig. 3*B*) photographs demonstrated higher reflectivity for shorter wavelengths in the atrophic region due to enhanced penetration of the light into the choroid. The fundus AF (Fig. 3*C*) depicted a well-defined area lacking fluorescence (dark zone) corresponding to the area of GA (16). The early phase of FA (Fig. 3*D*) shows a somewhat blurred outline of the deeper larger choroidal vessels in the area of GA likely due to loss of the overlying CC. The pvOCT images, however, show well-defined capillary networks in the retina (Fig. 3*E*) and the inner choroidal layer (Fig. 3*F*) with focal disruption/loss of CC within the area of GA. Here, segmentation of the inner choroidal layer was ~6 μm beneath the RPE from the volumetric fly-through video (Movie S3). Increased penetration of the infrared light source into the choroid enabled the visualization of larger choroidal vessels (Fig. 3*G*) at the outer Haller's layer without the use of the inversing minimum projection method presented earlier. Here, the diameter of the larger vessel is ~168 μm at the red arrow. Furthermore, the green dotted line (Fig. 3*G*), delineating deeper vasculature areas from surrounding dimmer areas agrees with the atrophic area from the clinical images (Fig. 3 *A*–*C*).

To demonstrate changes in the CC in the normal appearing retina surrounding GA, we acquired a large field of view OCT scan (6° inferior retina eccentricities) covering atrophic and healthy regions of the macula from the same GA patient. The color fundus (Fig. 4*A*) and AF (Fig. 4*B*) images show two regions of GA. An *en face* projection (Fig. 4*E*) of CC segmented ~6 μm underneath the RPE (Movie S4) indicated focal patches of CC atrophic regions and were marked by green arrowheads. The combined pseudocolor coded image of retinal vessels (Fig. 4*D*, red) and CC (Fig. 4*E*, green) allows discrimination of remaining and damaged regions of CC. The diameter of hexagonally arrayed capillaries denoted by two red arrows is ~24 μm. The estimated size of the CC at the macula is comparable to measurements taken from another subject at the same region (Fig. 1). The diameter of these capillaries is expected to increase as the location moves toward the peripheral retina, as is demonstrated by the measurements of ~40 μm shown in Fig. 2. This trend is in agreement with previous histopathological studies (15).

Depth Locations of Vasculature in the Posterior Eye. Two-dimensional clinical fundus images can, in general, classify atrophic AMD according to optical reflectivity differences (8). A unique feature of our noninvasive technique is that the pvOCT images provide the depth of the vascular abnormalities and associated structural changes. To evaluate the capabilities of OCT intensity and pvOCT data in the identification of vascular circulation within B-scans, composite images of these two imaging methods have been compared at normal (Fig. 5 *A*–*D*) and GA (Fig. 5 *E*–*H*) regions. The OCT intensity cross-sectional scan (Fig. 5*A*) provides identification of retinal and choroidal layers; larger retinal and choroidal vessels can also be observed, indicated by the orange arrowhead and the white arrow, respectively. Medium diameter blood vessels, indicated by purple arrowheads (Fig. 5*C*) in Sattler's layer, can be identified and are positioned between the CC and the outermost choroid layer. However, within conventional OCT intensity images, it is challenging to separate retinal and choroidal microcapillaries from neighboring bright structures. Unlike the OCT intensity image, the combined B-scan (Fig. 5*B*) with phase-variance processing emphasizes depth locations of capillaries (red). The magnified image (Fig. 5*D*) demonstrates blood perfusion in the inner choroid layer where green arrows denote phase-variance signals from the CC underneath Bruch's membrane. The averaged OCT B-scan (Fig. 5*E*) shows loss of photoreceptor cells at the blue arrow in the fovea, resulting in a central blind spot. Red arrows compare the deeper OCT depth penetration region of the atrophy to the non-enhanced beam penetration area. The composite image (Fig. 5*F*) with pvOCT indicates locations of vasculature and the zoomed-in position (Fig. 5*H*) of the yellow dashed rectangle.

Discussion

Depth-resolved vascular imaging in the eye with pvOCT has several advantages for clinical diagnostic and research settings, particularly with regards to visualization and convenience. High-resolution 3D microvascular imaging capabilities of pvOCT allows for virtual segmentation of the retinal and choroidal layers, providing opportunities to observe subtle changes in the microvasculature during the progression and treatment of ocular diseases. In addition, pvOCT is able to visualize vasculature independent of regional leakage due to contrast differences. With this capability, vascular response to antiangiogenic therapeutics can be directly visualized, even in the presence of leakage, which might impact other angiography methods. The noninvasive nature of this imaging method permits more frequent use than

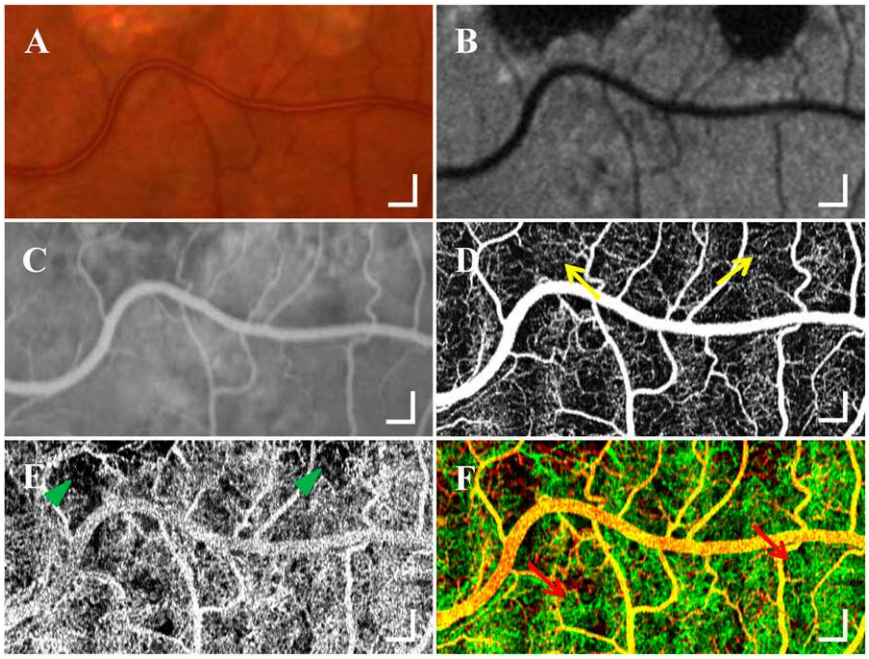

Fig. 4. Identification of abnormality in CC at edges of GA for a scanning area of 3 × 1.5 mm^2. Selected regions of color fundus photograph (*A*), AF (*B*), and an early phase of FA (*C*) from the location identified by the purple dotted rectangle (Fig. S5). An *en face* image (*D*) from pvOCT data shows fine normal retinal capillaries (yellow arrows) at the edge of GA, which are not as well visualized with FA (*C*). A CC perfusion map (*E*) from pvOCT illustrates small focal areas of CC dropout near the inferior edge of GA, which correlates with the areas of irregular choroidal filling on FA (*C*). A color composite image (*F*) of retinal circulation (*D*, red) and CC (*E*, green) from pvOCT. (Scale bars, 200 μm.)

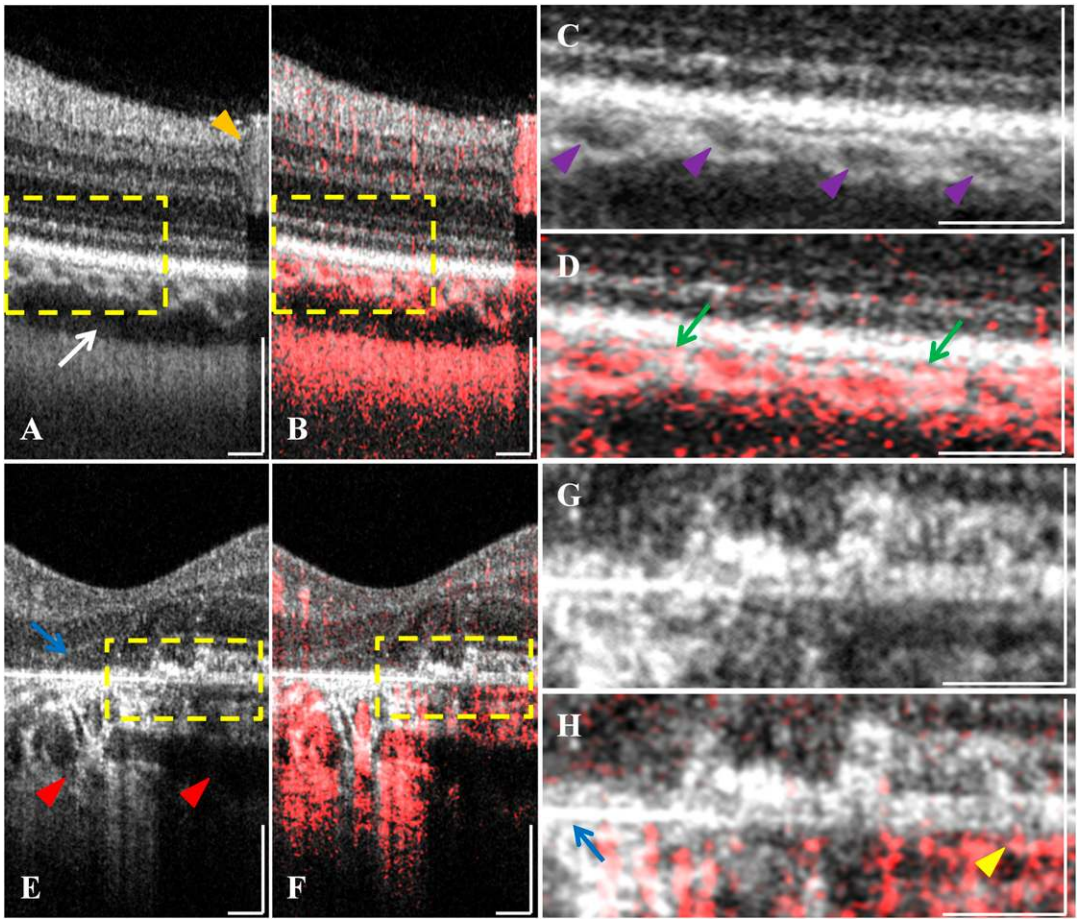

Fig. 5. Depth-resolved image of capillaries in the retina and the choroid. A standard OCT cross-sectional scan (*A*) averaging three B-scans within a BM-scan (multiple B-scans at the same position) and a composite image (*B*) of the OCT B-scan (gray) and pvOCT image (red). The retinal position of Fig. 5 *A*–*D* is identified on the vertical yellow dashed line in Fig. 2*D*. Magnified version of OCT intensity (*C*) and composite imaging (*D*) cropped from the location indicated at the yellow dashed rectangles in *A* and *B*. An OCT B-scan (*E*) and a pvOCT red-coded image (*F*) of the patient with GA, with a retinal scan location as identified on the horizontal yellow dashed line Fig. 3*D*. Cropped images (*G* and *H*) from the location of the yellow dashed rectangles in *E* and *F*. As indicated by the blue arrow (Fig. 5*H*), the phase-variance signals by microcirculation disappeared underneath Bruch's membrane due to CC atrophy, whereas motion contrast signals by blood perfusion (remaining CC) exist in the region pointed by the yellow arrowhead. Volumetric imaging of color-coded B-scans from above two datasets is included (Movies S5 and S6). Horizontal image size for *A*, *B*, *E*, and *F*: 1.5 mm. (Scale bars, 200 μm.)

clinical angiography techniques currently used. This creates opportunities for monitoring long-term vascular disease progression as well as for early disease detection, an option that is limited by the invasiveness of the injectable dyes used in clinical angiography.

As mentioned previously, one of the limitations of this imaging method is the shadow artifacts observed deep to the retinal vasculature. This type of artifact is a byproduct of pvOCT contrast, which calculates the variance over time of phase changes for scatterers in the retina and choroid. Because phase is dependent on the optical path traveled by the imaging light, changes in phase can be caused by positional changes of the scatterer or by changes in the index of refraction of the optical path the light has traveled. Below regions of major vasculature, it is difficult for pvOCT to differentiate between variations in scattering positions and variances in the index of refraction of the region of flow, which creates the artifacts identified previously.

Within OCT imaging of the choroid, signal is noticeably absent within the largest choroidal vessels (17). We suspect that fast flow rates of these vessels induce fringe washout of spectrometer-based OCT signals and cause the signal to drop below the noise level of the system. In that case, the loss of OCT intensity signal within these blood vessels also creates a lack of phase-shift information and pvOCT signal (18). To address this issue, we have applied a similar methodology to the visualization of choroidal vessels by an inversed minimum projection view of the phase-variance processed data segmented over Haller's layer (Fig. 1*F*).

This study has demonstrated some of the capabilities of pvOCT for microvascular imaging in the posterior eye, bringing the potential for in vivo identification of vascular degeneration and atrophy in the choroid. These results establish that this modality may provide an opportunity for diagnosing choroidal vascular abnormalities, including those occurring in GA, and may potentially be useful for studying changes in CC associated with exudative AMD, before and after antiangiogenic therapy. This noninvasive vasculature imaging technique is a software solution that can be implemented in clinically available OCT systems without any hardware modification, which is beneficial for translational research and further clinical applications. The pvOCT method holds the potential to revolutionize the field of choroidal vascular diagnostics and treatment.

Methods

Human Subject Imaging. This research observed the tenets of the Declaration of Helsinki. Written informed consent was obtained after all procedures were fully explained, and before experimental measurements. The consent was approved by the institutional review board at the University of California, Davis School of Medicine.

Fundus Photography. Color and red-free fundus photographs (50° field of view) were acquired with a Topcon (TRC-50IX) camera having resolution of 1,280 (horizontal, H) × 1,024 (vertical, V) pixels. The color photographs were acquired from full red, green, blue (RGB) color imaging with white light illumination from a xenon lamp. The red-free photographs were obtained with a green filter to remove long wavelengths. For fluorescein angiography, sodium fluorescein 10% in water (500 mg/5 mL) was injected intravenously using a 23- or 25-gauge needle, followed by a flush of normal saline. Either the TRC-50IX or the Spectralis (HRA + OCT, trademarked product of Heidelberg Engineering) were used for FA imaging. The images consisted of 1,536 (H) × 1,536 (V) pixels over 30° acquired at a 40-kHz scanning rate with a confocal scanning laser ophthalmoscope (cSLO). A 488-nm wavelength laser with 300 μW power excites the fluorescein, together with a barrier filter at 500 nm to separate the excitation and emission light. ICGA imaging was obtained after i.v. injection of 25 mg in 5 mL of aqueous diluent and then after flushing the line with 5 mL normal saline i.v. A diode laser at 790 nm and an 830-nm filter were used for excitation of ICG and blocking the excitation light, respectively. In addition, AF acquired endogenous fluorescence reflectance imaging by excitation from the 488 nm light. ICGA and AF images were acquired with the Spectralis HRA + OCT. All these clinical images were taken with fully dilated pupils. These procedures, imaging systems, and contrast dyes are approved by the Food and Drug Administration.

OCT Imaging. A schematic of the OCT system is shown in Fig. 6. The light source is a superluminescent diode (D855; Superlum Diodes) with a center wavelength of 855 nm, bandwidth of 75 nm, allowing axial resolution of 4.5 μm in the retina (refractive index, $n = 1.38$). The transverse resolution at the retina is estimated at 10–15 μm depending on the subject's ocular aberrations. The measured light power at the pupil is 700 μW, which is below the safety limit of the American National Standards Institute (19) and the maximum sensitivity of the system is ∼100 dB. The fixation target was viewed through a dichroic beamsplitter. A fiber coupler (AC Photonics) with an 80/20 splitting ratio sends 20% of the input light to the sample arm and 80% to the reference arm containing glass matched to the dispersion of water. An isolator prevents back reflection of the light to the source. The galvanometer mirrors (6200H; Cambridge Technology) are used for X–Y scanning. A purpose-built spectrometer consisted of a 12-bit line scan camera (spL4096, 140 km; Basler AG) with 4,096 pixels, a 150-mm objective lens, and a 1,200 L/mm diffraction grating (20). The imaging speed in this study was 125 KHz using 2,048 active pixels. The rapid-speed frame grabber (PCIe-1429; National Instruments) acquires interference fringe patterns from the camera, and custom-made software written in LabVIEW (National Instruments) supports standard Fd-OCT processing including spectral shaping (21), zero padding (22), and dispersion compensation (23). Imaging acquisition time for retinal area scans of 1.5 × 1.5 mm^2 and 3 × 3 mm^2 was 3.8 s and the 1.5 × 3 mm^2 and 3 × 1.5 mm^2 scans were acquired in 6.9 s. Image sampling density between successive A-scans (axial scans) and BM-scans is ∼4 μm for 1.5 × 1.5 mm^2 and 1.5 × 3 mm^2 scan patterns, and ∼8 μm for the 3 × 3 mm^2 scan pattern. A forehead rest and a bite bar were used to reduce head motion, while a liquid crystal display screen provided a fixation target to reduce eye motion artifacts. The eye pupil was not dilated for pvOCT imaging. Phase-variance processing (24, 25) of acquired volumetric data from human subjects is described in *Supporting Information*.

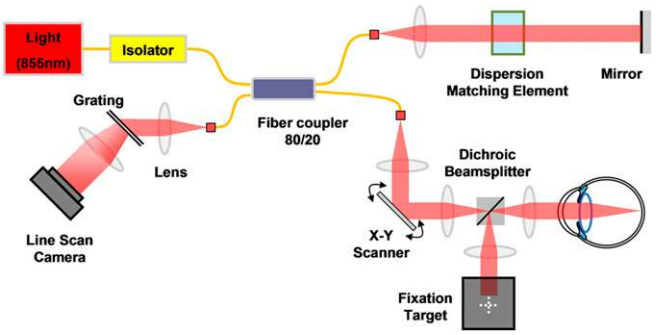

Fig. 6. Schematic of the OCT system. A fiber-based Michelson interferometer was used with an infrared light source having 855-nm central wavelength. The power of the collimated light at the pupil of the eye is 700 μW, below the safety limit of the American National Standards Institute. The light is focused onto the posterior eye, and the back-reflected light from the sample and the reference mirror are combined in the spectrometer portion of the interferometer, which uses a line-scan camera to acquire spectral fringes of the combined light. The Fourier transform of a single spectral fringe pattern generates depth information of a single point, both an intensity profile (axial scan or A-scan) and its phase profile. The X–Y scanner permits acquisition of 3D datasets over defined patches of retina.

ACKNOWLEDGMENTS. We thank R. H. Grubbs (Department of Chemistry, California Institute of Technology) for helpful discussions and support and S. Garcia (Vision Science and Advanced Retinal Imaging Laboratory, University of California, Davis Medical Center) for help with phase-variance optical coherence tomography data acquisition and acquiring fundus photographs. This research was funded in part by National Eye Institute Grant EY014743 (to J.S.W.), Research to Prevent Blindness (J.S.W., S.S.P., and L.S.M.), the Beckman Institute (S.E.F.), the That Man May See Foundation (D.M.S.), and Howard Hughes Medical Institute Med-into-Grad Initiative 56006769 (to D.Y.K.).

1. Forte R, et al. (2012) Multimodal imaging of dry age-related macular degeneration. *Acta Ophthalmol (Copenh)* 90(4):e281–e287.
2. Querques L, Querques G, Forte R, Souied EH (2012) Microperimetric correlations of autofluorescence and optical coherence tomography imaging in dry age-related macular degeneration. *Am J Ophthalmol* 153(6):1110–1115.
3. Friedman DS, et al.; Eye Diseases Prevalence Research Group (2004) Prevalence of age-related macular degeneration in the United States. *Arch Ophthalmol* 122(4):564–572.
4. Bird AC, et al.; International ARM Epidemiological Study Group (1995) An international classification and grading system for age-related maculopathy and age-related macular degeneration. *Surv Ophthalmol* 39(5):367–374.
5. McLeod DS, et al. (2002) Quantifying changes in RPE and choroidal vasculature in eyes with age-related macular degeneration. *Invest Ophthalmol Vis Sci* 43(6):1986–1993.
6. Sunness JS (1999) The natural history of geographic atrophy, the advanced atrophic form of age-related macular degeneration. *Mol Vis* 5:25.
7. Holz FG, Bellman C, Staudt S, Schütt F, Völcker HE (2001) Fundus autofluorescence and development of geographic atrophy in age-related macular degeneration. *Invest Ophthalmol Vis Sci* 42(5):1051–1056.
8. Brader HS, Ying GS, Martin ER, Maguire MG; Complications of Age-Related Macular Degeneration Prevention Trial-CAPT Research Group (2011) New grading criteria allow for earlier detection of geographic atrophy in clinical trials. *Invest Ophthalmol Vis Sci* 52(12):9218–9225.
9. Huang D, et al. (1991) Optical coherence tomography. *Science* 254(5035):1178–1181.
10. Wojtkowski M, Leitgeb R, Kowalczyk A, Bajraszewski T, Fercher AF (2002) In vivo human retinal imaging by Fourier domain optical coherence tomography. *J Biomed Opt* 7(3):457–463.
11. Fleckenstein M, et al. (2008) High-resolution spectral domain-OCT imaging in geographic atrophy associated with age-related macular degeneration. *Invest Ophthalmol Vis Sci* 49(9):4137–4144.
12. Spaide RF, Koizumi H, Pozzoni MC (2008) Enhanced depth imaging spectral-domain optical coherence tomography. *Am J Ophthalmol* 146(4):496–500.
13. Imamura Y, Fujiwara T, Margolis R, Spaide RF (2009) Enhanced depth imaging optical coherence tomography of the choroid in central serous chorioretinopathy. *Retina* 29(10):1469–1473.
14. Yoneya S, Tso MO (1987) Angioarchitecture of the human choroid. *Arch Ophthalmol* 105(5):681–687.
15. Olver JM (1990) Functional anatomy of the choroidal circulation: Methyl methacrylate casting of human choroid. *Eye (Lond)* 4(Pt 2):262–272.
16. Delori FC, et al. (1995) In vivo fluorescence of the ocular fundus exhibits retinal pigment epithelium lipofuscin characteristics. *Invest Ophthalmol Vis Sci* 36(3):718–729.
17. Povazay B, et al. (2009) Wide-field optical coherence tomography of the choroid in vivo. *Invest Ophthalmol Vis Sci* 50(4):1856–1863.
18. Hendargo HC, McNabb RP, Dhalla AH, Shepherd N, Izatt JA (2011) Doppler velocity detection limitations in spectrometer-based versus swept-source optical coherence tomography. *Biomed Opt Express* 2(8):2175–2188.
19. Delori FC, Webb RH, Sliney DH; American National Standards Institute (2007) Maximum permissible exposures for ocular safety (ANSI 2000), with emphasis on ophthalmic devices. *J Opt Soc Am A Opt Image Sci Vis* 24(5):1250–1265.
20. Kim DY, et al. (2011) In vivo volumetric imaging of human retinal circulation with phase-variance optical coherence tomography. *Biomed Opt Express* 2(6):1504–1513.
21. Nassif N, et al. (2004) In vivo high-resolution video-rate spectral-domain optical coherence tomography of the human retina and optic nerve. *Opt Express* 12(3):367–376.
22. Zawadzki RJ, et al. (2005) Adaptive-optics optical coherence tomography for high-resolution and high-speed 3D retinal in vivo imaging. *Opt Express* 13(21):8532–8546.
23. Wojtkowski M, et al. (2004) Ultrahigh-resolution, high-speed, Fourier domain optical coherence tomography and methods for dispersion compensation. *Opt Express* 12(11):2404–2422.
24. Fingler J, Zawadzki RJ, Werner JS, Schwartz D, Fraser SE (2009) Volumetric microvascular imaging of human retina using optical coherence tomography with a novel motion contrast technique. *Opt Express* 17(24):22190–22200.
25. Kim DY, et al. (2012) Noninvasive imaging of the foveal avascular zone with high-speed, phase-variance optical coherence tomography. *Invest Ophthalmol Vis Sci* 53(1):85–92.